JOURNAL OF MATERIALS SCIENCE 26 (1991) 2313–2321

Fracture mechanics model for subthreshold indentation flaws

Part II *Non-equilibrium fracture*

S. LATHABAI*, J. RÖDEL*, T. DABBS‡, B. R. LAWN
Ceramics Division, National Institute of Standards and Technology, Gaithersburg, MD 20899, USA

In Part II of this two-part study we extend the shear-fault–microcrack model to non-equilibrium fracture, to allow for rate effects in the critical instability configurations in chemically interactive environments. The "calibrated" *K*-fields of Part I are combined with independently evaluated crack velocity functions to determine kinetic conditions for microcrack extension. The analysis enables evaluation of (i) a time delay in radial crack pop-in from a subthreshold flaw; (ii) a time dependence in the strength characteristics, in both the subthreshold and postthreshold domains. Comparisons with delayed pop-in and strength–stressing-rate literature data for silicate glasses in moist environments indicate that the analysis is capable of quantitative predictions of kinetic characteristics. In the strength data, the model accounts for the relatively high magnitudes, scatter and fatigue susceptibilities in the subthreshold region.

1. Introduction

In Part I we developed a shear-fault–radial-crack model for the critical pop-in and associated strength properties of surfaces with indentation flaws under conditions of *equilibrium* fracture [1]. Now we extend the analysis to *non-equilibrium* fracture. In particular, we address the kinetics of delayed pop-in [2, 3] and rate-dependent strength degradation of Vickers-indented glass surfaces [4–9] on exposure to moist environments, phenomena of much relevance to the mechanical integrity of ultra-high-strength brittle components.

Our approach is straightforward. We use the equilibrium parametric fits to experimental data in Part I as a "calibration" of the residual-contact and applied-stress *K*-fields, and introduce the rate dependence through an independently determined crack velocity function $v = v[G(K)]$ (G is the mechanical energy-release rate). In this way we can predetermine the complete time evolution of microcrack growth in specified moisture-containing environments, with or without applied stress.

The model will be used to confirm the highly deleterious effects of water-containing environments in the subthreshold region. Specific attention will be directed to the observation that pop-in can occur from a subthreshold flaw well after completion of the indentation event, at loads lower than those for inert environments by as much as an order of magnitude; and that strength–stressing-rate (fatigue) curves for subthreshold flaws have significantly higher slopes than their postthreshold counterparts, with correspondingly greater scatter in data. It will also be used to explain differences in non-equilibrium fracture behaviour of normal (soda-lime) and anomalous (fused silica) glasses.

2. Incorporation of kinetics into fracture mechanics model

In this section we indicate how the *K*-field analysis of Part I may be combined with a crack velocity function to predict the kinetic aspects of crack initiation and strength.

2.1. *K*-fields

Recall from Part I the essence of our indentation shear fault model: that there exists a residual driving force, with shear and tensile components, on the post-indentation radial microcrack; and that this force is augmented by corresponding components from a subsequently applied external stress σ_A. The net driving force on the crack is given by Equation 1 in Part I

$$\begin{aligned} K(c, a, \beta, \sigma_A) = {} & Ha^{1/2}\{[\alpha_R^T f_R^T(c/a, \beta) \\ & + (\sigma_A/\sigma_1^0)\alpha_A^T f_A^T(c/a, \beta)]^2 \\ & + [\alpha_R^S f_R^S(c/a, \beta) \\ & + (\sigma_A/\sigma_I^0)\alpha_A^S f_A^S(c/a, \beta)]^2\}^{1/2} \end{aligned} \quad (1)$$

---

* *Guest Scientists*: On leave from the Department of Materials Science and Engineering, Lehigh University, Bethlehem, PA 18015, USA.
‡ *Present address*: CSIRO, Division of Wool Technology, Sydney, NSW 2112, Australia.

with c the crack size, a the indentation half-diagonal, β a normalized coordinate locating the shear fault within the contact impression; H the hardness and σ_I^0 a reference strength (Tables I and II, Part I); the α terms are coefficients which determine the intensity of the K-fields (Table II, Part I), and the f terms are crack-size functions (Equations 8, 9, 15 and 16, Part I).

2.2. Crack velocity functions for glasses

The first step in extending the model of Part I to non-equilibrium properties is to introduce suitable crack velocity functions for the glasses for which kinetic data are available, namely soda-lime and fused silica. There is a considerable literature on the velocity characteristics of these and other silicate glasses. Here we adopt a set of phenomenological relations which can be fitted to existing velocity data, and which can then be used to compute crack velocities in gaseous environments of any specified relative humidity and in water. The velocity relations for active environment assume the general functional form in the region $K < K_C = T_0$

$$v = v\{G[K(c)], R\} \qquad (2)$$

where R is relative humidity and G the mechanical-energy-release rate at the crack tip. These velocity functions connect to the K-field in Equation 1 via the familiar plane strain relation [10]

$$G = K^2(1 - \nu^2)/E \qquad (3)$$

where E is Young's modulus and ν Poisson's ratio. Details of the functions $v\{G[K(c)], R\}$, which embrace three regions of the v–G curve and (in soda-lime glass) exhibit a threshold, are given in the Appendix.

We also determine in the Appendix appropriate coefficients in the velocity functions by fitting to selected data for soda-lime glass and fused silica from the literature. It should be stated at the outset that v–G data are notoriously difficult to reproduce in absolute terms, and probably carry an uncertainty in velocity of at least an order of magnitude at any specified G value, even more so as we attempt to extrapolate the fitted curves beyond the measured data range.

2.3. Differential Equation for Kinetic Crack Growth

Now we combine the K-field and crack velocity relations into a formalism for non-equilibrium crack growth in the load–time fields $P(t)$ and $\sigma_A(t)$ shown in Fig. 1. The quantities T_1, T_2 and T_3 define the contact duration, post-indentation interval, and time to failure at constant applied stressing rate, respectively. The quantities t', $t'' = t' - T_1$ and $t''' = t'' - T_2 = t' - (T_1 + T_2)$ define time coordinates within these intervals. For $P(t)$, we assume a square pulse; for $\sigma_A(t)$, we consider the function $\sigma_A(t) = \dot{\sigma}_A t'''$ at stressing rates $\dot{\sigma}_A$ = constant ("dynamic fatigue").

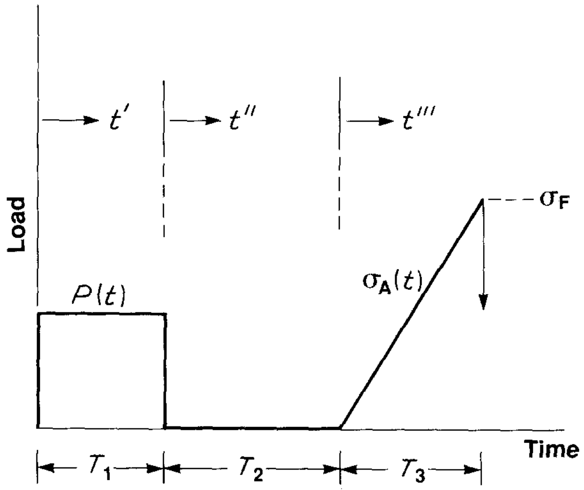

Figure 1 Schematic showing indentation load–time (P–t) pulse over duration T_1, subsequent post-indentation interval T_2, and ultimate applied stress–time (σ_A–t) loading to failure over T_3. Origins in time coordinates t', $t'' = t' - T_1$ and $t''' = t'' - T_2 = t' - (T_1 + T_2)$, measured from the start of contact, of the post-indentation interval, and the applied stress cycle, respectively. Configurations of interest are: "delayed" pop-in, $0 < t''_C < T_2$; "fatigue" strength σ_F at $t''' = T_3$, for postthreshold ($t''_C < T_2$) and subthreshold ($t''_C > T_2$) indentations.

Accordingly, Equations 1 to 3 lead to a differential equation of the general functional form

$$dc(t)/dt = v = F\{K[c(t), a, \beta, \sigma_A(t)], R\} \qquad (4)$$

This relation has to be solved for $c(t)$ at a given stress-time function $\sigma_A(t)$. We are specifically interested in two cases:

(i) *Pop-in*, $\sigma_A = 0$. In the absence of applied stress, chemistry can cause a subthreshold microcrack to pop-in some critical time t''_C after completion of the indentation cycle, under the action of indentation stresses alone. Again, we recall from Part I (Section 3.2) that there exists a dominant compressive stress component in the elastic contact field which effectively suppresses crack growth at peak contact load through the duration T_1[*], corresponding to an initial condition $t'' = 0$, $K_R = 0$ in the differential Equation 4. Then t''_C is evaluated as the time for a subcritical microcrack to grow from a shear fault at $c = \beta a$ (Fig. 3, Part I) in the full post-indentation K_R-field to final instability at $K_R = K_C = T_0$, $dK/dc > 0$.

(ii) *Strength*, $\sigma_F = \dot{\sigma}_A T_3$ at stressing rate $\dot{\sigma}_A$ = constant, corresponding to conditions under which "dynamic fatigue" strengths are measured. The post-indentation crack is allowed to evolve an amount Δc in the residual field during the interval T_2 prior to strength testing. (This growth stage turns out to be significant in the ultimate strength evaluation only as one approaches the intermediate, subthreshold activated region of Fig. 9 in Part I.) For *subthreshold* indentations, the solution is evaluated as the time T_3 for the microcrack initially at $t''' = 0$, $\sigma_A = 0$ to grow from $c = \beta a + \Delta c$ at prescribed $\dot{\sigma}_A$ to final failure; for

---

[*] This elastic compressive component actually reduces below its residual tensile counterpart at some point on the unloading half-cycle (at $\approx$ 0.3 peak load in soda-lime glass [3]; we avoid such complication by considering only a square load–time pulse, as indicated in Fig. 1.

postthreshold indentations, the procedure is the same but the initial crack size is determined as $c = c_2 + \Delta c$ (Fig. 7, Part I).

2.4. Numerical algorithm for solution of differential equation

The differential Equation 4 has no general analytical solution for the multi-region velocity functions defined in the Appendix. We use a numerical algorithm to increment crack size c and time t in a Runge–Kutta stepwise integration procedure, in accordance with prescribed sets of parameters T_1, T_2, a, β, σ_A, appropriately adjusting $K(c, t)$ at each step. The particular incrementing procedures used to handle the great range of crack velocities encountered in the typical evolution to failure is a modification of those described in an earlier study on the fatigue properties of indentation flaw systems [11].

An important element in our algorithm is the provision to allow properly for multiple pop-in instabilities in the crack evolution. For delayed pop-in under the action of the residual field K_R alone, i.e. case (i) in the preceding subsection, there is just one such instability. For crack growth in the superposed field of the subsequently applied stress, case (ii) above, the possibility exists for an intermediate jump–arrest stage, followed by an interval of stable growth, in the evolution to failure. Accordingly, a routine which continues to test for the instability condition $\mathrm{d}K/\mathrm{d}c > 0$ after each pop-in stage is used to ensure that an unlimited failure configuration is attained.

3. Comparison of theory and experiment

Now we compare predictions from the "calibrated" differential equation, i.e. using K-field parameters from the equilibrium data fits in Part I and crack velocity parameters from the independent data fits in the Appendix, with observed radial crack pop-in and strength data for soda-lime and fused silica glasses in moist environments.

3.1. Delayed pop-in

Experimental data $t''_C(a)$ for delayed pop-in for the two glasses [2, 3, 12] are shown in Fig. 2. These data were taken using a square $P(t)$ indentation load pulse, at prescribed contact durations T_1, in accordance with the theoretical prescription in Fig. 1. The indentations were made in nitrogen (inert), air (50% relative humidity) and water, and maintained in those environments until pop-in occurred. Each data point in Fig. 2 is a 50% cumulative probability value. Data scatter bands are considerable, ranging over as much as two orders of magnitude in time at ± 25% probability bounds, and are therefore omitted from the plots for clarity. The data for fused silica relative to soda-lime in air reflect a characteristic difference between the two glass types: in anomalous glasses pop-in is much more abrupt – it tends to occur almost immediately on completion of indentation or not at all. In nitrogen, any persistent kinetic effect is attributable to trace water vapour.

The theoretical fits for each glass and environment are generated as described in the previous section, for mean $\beta = 0.923$. (Comparative plots using extreme values $\beta = 0.846$ and 1 indicate a wide scatter in pop-in times, consistent with the experimental observation, but are again omitted from Fig. 2 for clarity.) Especially notable are the order-of-magnitude reductions in the critical pop-in loads in moist air relative to nitrogen; these reductions are even greater in water (and may be reduced still further in acidic aqueous solutions [13]). Note also the tendency to a cutoff load below which pop-in does not occur, especially abrupt for fused silica, in accordance with the experimental observation.

At the same time, notwithstanding the scatter in the data, there are apparent discrepancies between theory and experiment, notably in soda-lime glass, that bear mention. First, the data set for the water curve lies well below the predicted curve. Second, the data set for air at the shortest contact duration ($T_1 = 0.1$ s) appear to fall systematically above the predicted curve. These trends imply that time and chemistry, factors that we

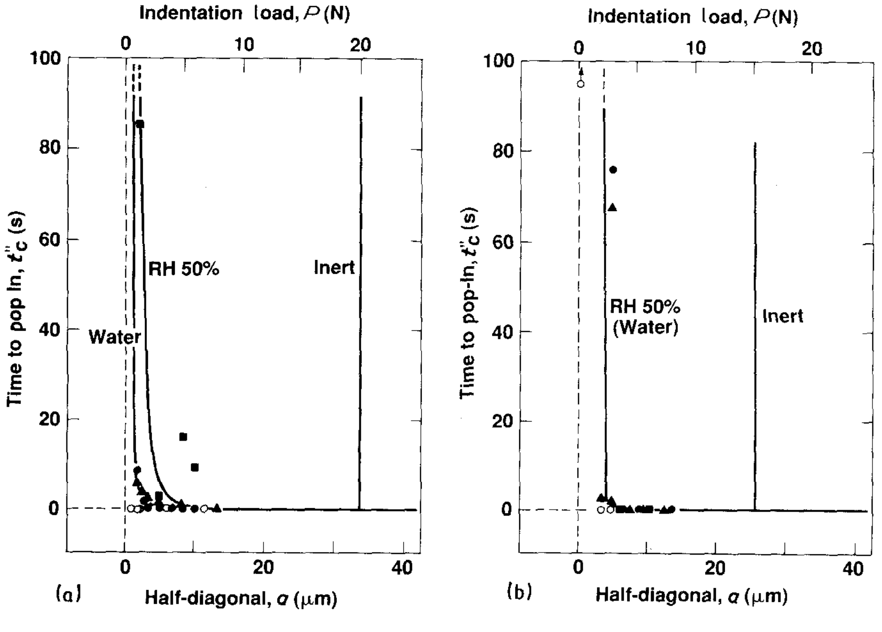

Figure 2 Delayed pop-in for (a) soda-lime glass and (b) fused silica in different environments [2, 3, 12]. Data are 50% cumulative probability values. Tests in air (50% RH) (closed symbols) at $T_1 = 10$ s (●), $T_1 = 1.0$ s (▲) and 0.1 s (■); in water (open symbols) at $T_1 = 10$ s; nitrogen (data not included, owing to excessive scatter on time axis). Arrows indicate interrupted tests. Full curves are theoretical predictions, for $\beta = 0.923$. (Predicted curves for air and water indistinguishable in (b).)

have explicitly assumed to be passive *during contact*, must play some role in the development of the residual K-field. We shall return to these factors in the discussion.

3.2. Strength–stressing-rate curves

The most common test procedure for evaluating environmental rate effects in lifetimes of intrinsically brittle solids, in the context of indentation as well as natural flaws, is that of so-called "dynamic fatigue"; i.e. strength as a function of stressing rate. Such strength data are available for subthreshold and postthreshold Vickers indentation flaws in soda-lime and fused silica glasses tested in water [4–9, 14, 15].

We plot those experimental results as mean and standard deviation data points in Figs 3 to 6. The indentations in all these cases were made at a contact duration $T_1 \approx 10$ s and left for an interval $T_2 \approx 60$ min in air before strength-testing in water. The soda-lime data were taken exclusively on rod specimens; the fused silica postthreshold data on rods, subthreshold on fibres. For subthreshold tests, it was necessary to use indentation loads below the cut off limits in air in Fig. 2, to guard against premature pop-in prior to strength testing.

The curves in Figs 3 to 6 are predictions using the numerical algorithm, at $\beta = 0.923$ (full curves) and $\beta = 0.846$ and 1 (broken curves). At high stressing rates the curves saturate at the inert strength levels, as required. At low stressing rates the predicted curves tend to flatten out again: for both subthreshold flaws (Fig. 3) and postthreshold flaws (Fig. 4) in soda-lime glass this flattening is associated with a true threshold in the v–G curve (Fig. A1); for the subthreshold flaws in fused silica (Fig. 5) the flattening is associated with a suppression of the pop-in instability. We shall elaborate on these limiting regions in the discussion.

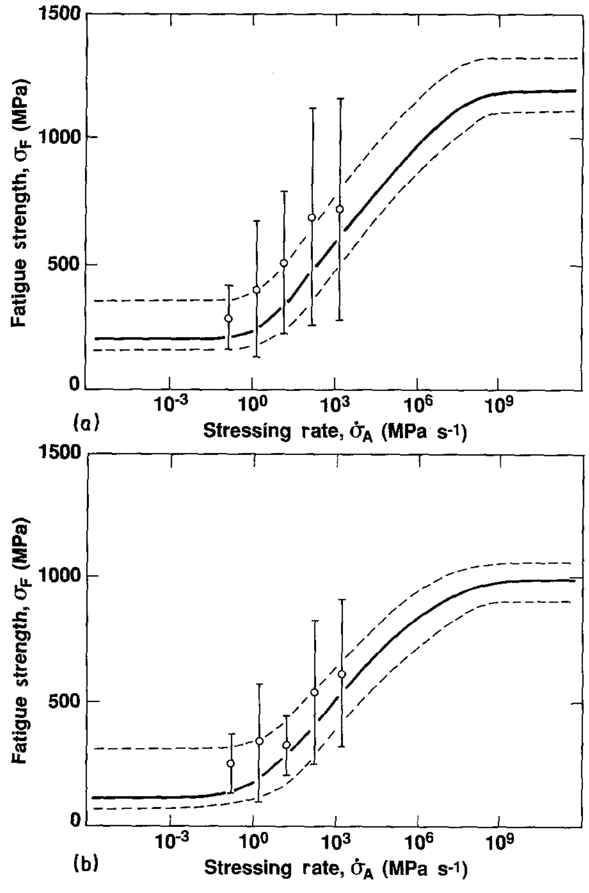

Figure 3 Fatigue strength plotted against stressing rate for *subthreshold* Vickers indentation flaws in soda-lime glass in water (after ageing in air for 60 min): (a) $a = 3.7$ μm ($P = 0.15$ N), (b) $a = 4.8$ μm ($P = 0.25$ N). Data means and standard deviations [5]. Curves are theoretical predictions, $\beta = 0.923$ (solid), 0.846 and 1 (broken).

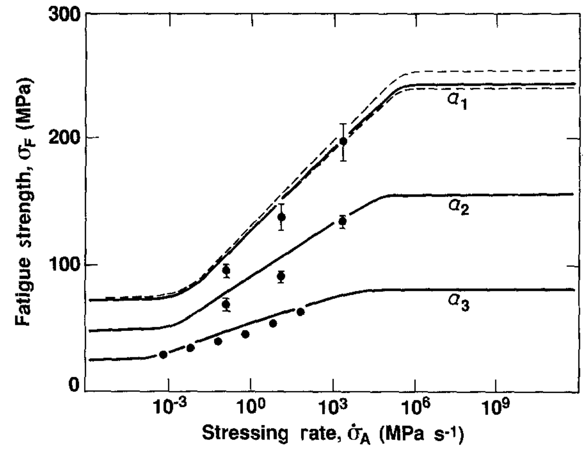

Figure 4 Fatigue strength plotted against stressing rate for (quasi-) *postthreshold* Vickers indentation flaws in soda-lime glass in water (after ageing in air for 60 min, during which interval pop-in occurs), at $a_1 = 4.3$ μm ($P = 0.20$ N), $a_2 = 8.0$ μm ($P = 0.70$ N), $a_3 = 21.3$ μm ($P = 5.0$ N). Data means and standard deviations [4, 14]. Curves are theoretical predictions: $\beta = 0.923$ (solid); 0.846 and 1 (broken), shown for a_1 curve only.

There are clear discrepancies between some of the *absolute* theoretical predictions and experimental results in Figs 3 to 6. Notwithstanding these discrepancies, the predictions are in accord with the major *trends* in the data. As with the inert strength data in Part I, the strengths of specimens with subthreshold flaws remain distinctly higher than their postthreshold counterparts, and the corresponding scatter is greater. In addition, (with due allowance for the different strength axes in Figs 3 and 5 as opposed to Figs 4 and 6) the slopes of the curves are greater in the subthreshold regions, consistent with the reportedly enhanced fatigue susceptibility of pristine as opposed to non-pristine glass fibres [16–18].

4. Discussion

In this study we have extended the model of Part I to include chemically enhanced rate effects in the fracture mechanics of indentation flaws. The extended model, with suitable incorporation of an independently determined crack velocity function, allows us to make predictions of (i) delayed radial-crack pop-in times for flaws in the subthreshold region, and (ii) the corresponding strength characteristics at prescribed stressing rates ('fatigue'). With regard to strength in particular, we are able to account for the relatively high magnitudes, error bars and susceptibilities that distinguish the subthreshold from its counterpart postthreshold domain.

In making these predictions, we are reliant on the accuracy of the calibrations of the α terms in the

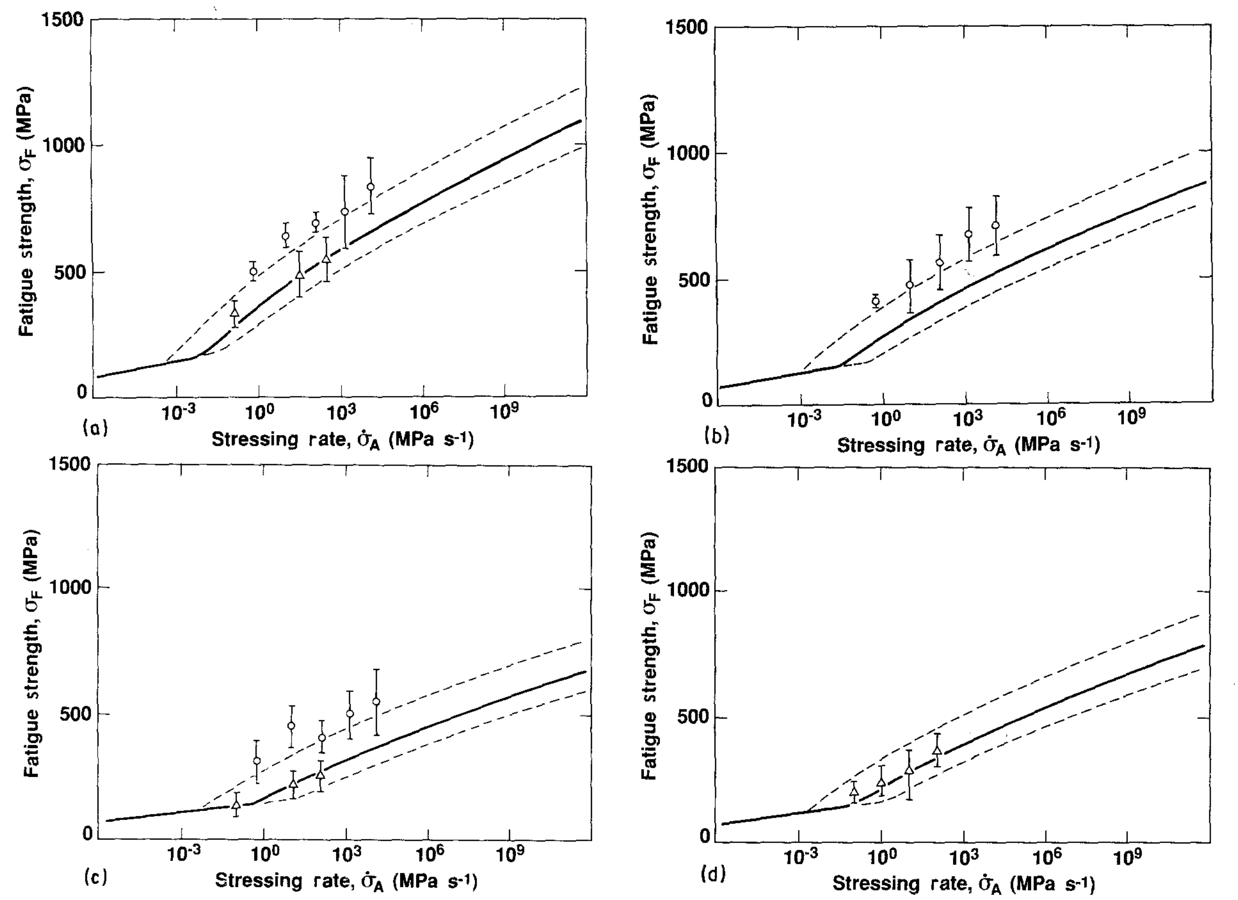

Figure 5 Fatigue strength plotted against stressing rate for *subthreshold* Vickers indentation flaws in fused silica glass in water (after ageing in air 60 min): (a) $a = 3.3$ μm ($P = 0.15$ N), (b) $a = 4.2$ μm ($P = 0.25$ N), (c) $a = 5.0$ μm ($P = 0.35$ N), (d) $a = 6.0$ μm ($P = 0.50$ N). Data means and standard deviations; ○ [8] and △ [9]. Curves are theoretical predictions, $\beta = 0.923$ (solid), 0.846 and 1 (broken).

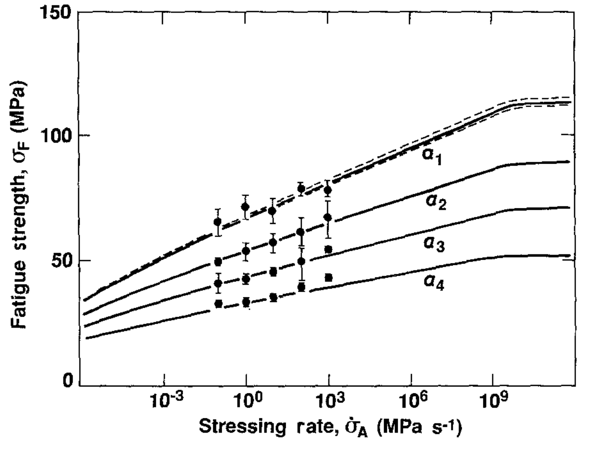

Figure 6 Fatigue strength plotted against stressing rate for *post-threshold* (and quasi-postthreshold) Vickers indentation flaws in fused silica glass in water (after ageing in air 60 min), indentation flaw sizes $a_1 = 18.2$ μm ($P = 5$ N), $a_2 = 26.7$ μm ($P = 10$ N), $a_3 = 37.8$ μm ($P = 20$ N), $a_4 = 60.0$ μm ($P = 50$ N). Data means and standard deviations [8]. Curves are theoretical predictions: $\beta = 0.923$ (solid); 0.846 and 1 (broken), shown for a_1 curve only.

K-field expressions in Part I, and, more importantly, of the parameters in the independently determined velocity functions in the Appendix. We have already indicated that reproducibility in velocity data to better than an order of magnitude is generally not feasible, even within the range of available data – it is well documented that extrapolations beyond the data range can lead to even greater uncertainties in lifetime predictions [19]. Such uncertainties, coupled with the sensitivity of the mechanics to geometrical details in the near-contact region could account largely for the observed discrepancies between experimental data and theoretical predictions, and cast doubt on the validity of the theoretical predictions at the low end of the $\dot{\sigma}_A$ range in Figs 3 to 6. Accordingly, whereas the analysis usefully predicts most of the important general trends in the pop-in and strength characteristics, it should be seen as somewhat restricted in its ability to predetermine absolute values.

Keeping these qualifications in mind, we may now use the differential equation algorithm to extract more detailed information on the kinetics of radial crack evolution during the post-indentation interval and the subsequent applied stressing to failure. Thus, we generate representative c against t curves for delayed pop-in at selected indentation sizes, Fig. 7; and for fatigue strength, at selected indentation sizes and stressing rates, Fig. 8. These diagrams delineate regions of instability as vertical discontinuities, and distinguish premature pop-in (single arrows) from unlimited failure (double arrows) during strength testing. Consider these two diagrams separately:

(i) In Fig. 7, we note that the subthreshold flaws at the smallest indentations sizes (a_1 and a_2 in Fig. 7a; a_1, a_2 and a_3 in Fig. 7b) show imperceptible growth over the time range plotted, but that the larger flaws all pop-in within the interval $T_2 = 60$ min between indentation and subsequent strength test, Section 3.2.

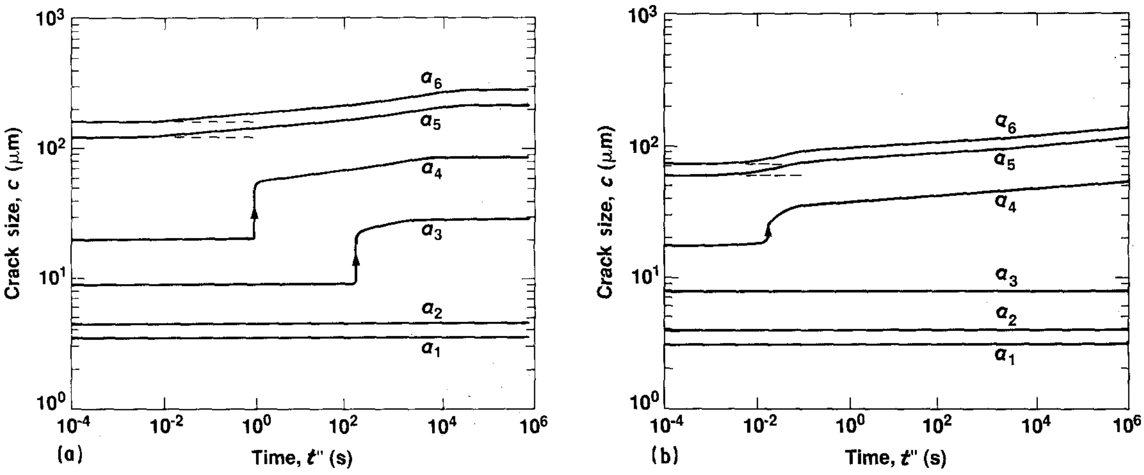

Figure 7 Predicted crack length c plotted against time t'' (see Fig. 1) for Vickers indentation flaws in silicate glasses in air (50% RH), under exclusive action of residual contact stresses. Calculations for several values of a, $\beta = 0.923$: (a) soda-lime, $a_1 = 3.7\ \mu m$ ($P = 0.15$ N), $a_2 = 4.8\ \mu m$ ($P = 0.25$ N), $a_3 = 9.5\ \mu m$ ($P = 1.0$ N), $a_4 = 21.3\ \mu m$ ($P = 5.0$ N), $a_5 = a^* = 42.6\ \mu m$ ($P = 20.0$ N), $a_6 = 52.2\ \mu m$ ($P = 30.0$ N); (b) fused silica, $a_1 = 3.3\ \mu m$ ($P = 0.15$ N), $a_2 = 4.2\ \mu m$ ($P = 0.25$ N), $a_3 = 8.5\ \mu m$ ($P = 1.0$ N), $a_4 = 18.9\ \mu m$ ($P = 5.0$ N), $a_5 = a^* = 32.7\ \mu m$ ($P = 15.0$ N), $a_6 = 37.8\ \mu m$ ($P = 20.0$ N). Horizontal dashed lines denote immediate post-indentation starting crack size. Vertical arrowed sections of full curves denote pop-in at $K_R = K_C = T_0$. Note small scale of radial crack extensions ($\Delta c = c - \beta a \ll a$) prior to instability.

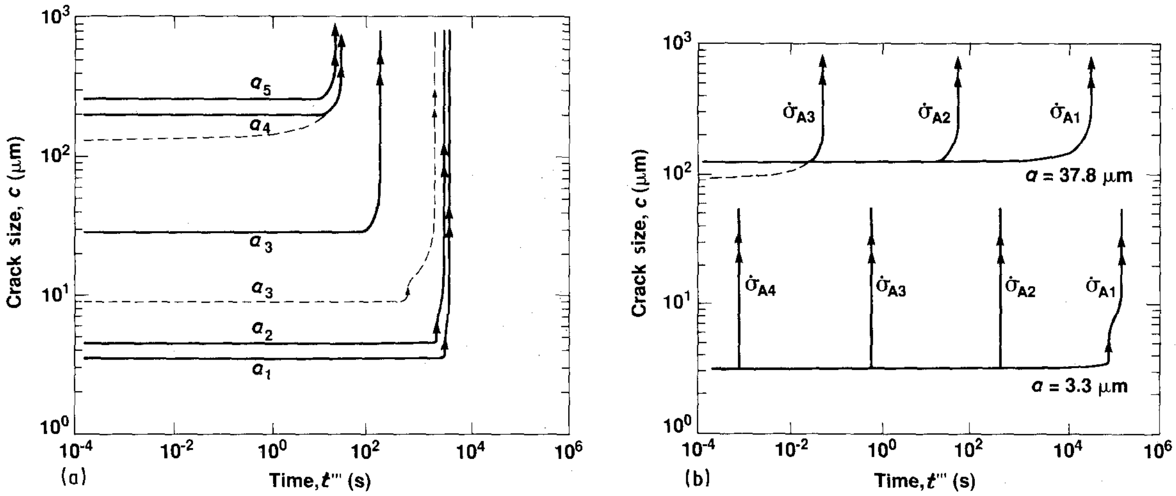

Figure 8 Predicted crack length c plotted against time t''' (see Fig. 1) for Vickers indentation flaws in water, under combined action of residual contact and externally applied stresses. Full curves are for flaws aged in air, $T_2 = 60$ min.; broken curves are for equivalent flaws strength-tested immediately on completion of indentation (hypothetically, at $T_2 = 0$). Calculations at $\beta = 0.923$: (a) soda-lime at fixed stressing rate $\dot{\sigma}_A = 10^3\ \mathrm{MPa\,s^{-1}}$ and variable indentation size, $a_1 = 3.7\ \mu m$ ($P = 0.15$ N), $a_2 = 4.8\ \mu m$ ($P = 0.25$ N), $a_3 = 9.5\ \mu m$ ($P = 1.0$ N), $a_4 = a^* = 42.6\ \mu m$ ($P = 20.0$ N), $a_5 = 52.2\ \mu m$ ($P = 30.0$ N); (b) fused silica at fixed indentation sizes $a = 3.3\ \mu m$ ($P = 0.15$ N) (subthreshold) and $37.8\ \mu m$ ($P = 20$ N) (postthreshold), and variable stressing rate, $\dot{\sigma}_{A1} = 10^{-3}\ \mathrm{MPa\,s^{-1}}$, $\dot{\sigma}_{A2} = 1\ \mathrm{MPa\,s^{-1}}$, $\dot{\sigma}_{A3} = 10^3\ \mathrm{MPa\,s^{-1}}$, $\dot{\sigma}_{A4} = 10^6\ \mathrm{MPa\,s^{-1}}$. Intermediate pop-in designated by single arrow, unlimited failure by double arrow.

The pop-in time diminishes rapidly towards zero as indentation size a approaches a^0 and ultimately exceeds the critical value a^*. These results illustrate graphically why flaws in the immediate size region $a < a^0$ tend to revert so readily to the postthreshold strength domain (Section 4.2, Part I).

(ii) In Fig. 8a the action of a linearly increasing applied stress enhances the crack growth rate, thereby diminishing the pop-in time (cf Fig. 7a), and generates a second, unlimited (failure) instability. The curves at $a > a^*$ with spontaneous pop-in and at $a < a^*$ with intermediate pop-in (activated failure) fall in the postthreshold strength domain. The curves at $a \ll a^*$ lie in the true subthreshold strength domain. In Fig. 8b we note the tendency for the subthreshold cracks at $a \ll a^*$ to extend over substantially greater subcritical distances as the stressing rate $\dot{\sigma}_A$ diminishes, equivalent to a transition in failure path from the first to the second stable branch of the $K(c)$ function in Fig. 8c of Part I. This transition is commensurate with the flattening out of the fused silica strength data at low $\dot{\sigma}_A$ noted earlier in Fig. 5.

In setting up the kinetic differential equation in Section 2.3 we assumed that microcrack extension is effectively suppressed during contact, owing to a dominant elastic compressive component in the indentation field at peak load. We also noted, however, that the delayed pop-in data for our glasses in Fig. 2 do show some dependence on contact duration; in particular, the soda-lime data in air at $T_1 = 0.1$ s appear to lie systematically above, and the data for water systematically below, the theoretical predictions. In the context of the air data, it has been observed that radial crack pop-in may be suppressed altogether as the (fixed-load) contact approaches (quasistatic) impact times [2]. There are strong implications here concerning potential rate effects in the shear fault configuration itself, which we have ignored in our model (recall, for instance, our unconditional assumption in Part I that the critical shear fault extends fully to the indentation diagonals, regardless of contact time). In practice, it is observed that the indentation *size* (e.g. as reflected in the hardness [20–22]) and *shape* [3] are both functions of contact time. Qualitatively, the indentation deformation zone is more developed, with attendant higher residual field intensity, at longer contact times. On the other hand, subsequent relaxation processes, e.g. as manifested in the time-dependent recovery of the hardness impression [21] and the growth of subsidiary (e.g. lateral) crack systems [14], can *reduce* the field intensity in the *post*-indentation period. Incorporation of such additional kinetic elements into the shear-fault–microcrack micromechanics could go some way to explaining our discrepancies.

Another point of interest is the difference in response of normal and anomalous silicate glasses. Soda-lime and fused silica glasses have similar hardness and toughness properties; yet differences in kinetic responses are manifest in the results presented here. Special reference may be made to the cut offs in the t''_C–a data in Fig. 2. The relative abruptness of this cut off for fused silica is partly due to the steeper v–G curve, but more importantly to the considerably weaker tensile component of the residual stress field (as reflected by the considerably more shallow $K_R(c)$ function for fused silica in Fig. 11 in Part I relative to that for soda-lime in Fig. 10), characteristic of materials whose constitutive deformation process contains a non-volume conserving component [23, 24].

The generality of the formalism used to describe the model in the two parts of this study should be noted. Extension to other brittle materials which exhibit similar shear deformation characteristics in indentation, e.g. quartz [3] and sapphire [25], should be possible. The essential ingredients for an appropriate fracture mechanics model remain the same: an appropriate K-field calibration (as in Part I); and an independently determined crack velocity function.

5. Conclusions

The conclusions are as follows:

(1) The shear-fault–microcrack model in Part I has been extended to include kinetics.

(2) By incorporating an independently determined crack velocity function into the calibrated indentation K-field relations from Part I, a differential equation for predicting the kinetics of radial crack initiation and propagation has been obtained.

(3) Predictions of the times for delayed radial crack pop-in from subthreshold Vickers indentations in soda-lime and fused silica glasses in specified moist environments have been compared with experimental data.

(4) Predictions of the rate dependence of strength as a function of stressing rate for indented soda-lime and fused silica glasses in water have been compared with experimental data, in both the subthreshold and postthreshold flaw domains.

(5) The predictions account for the essential data trends in the subthreshold as opposed to postthreshold strength data, notably higher strengths, greater scatter and increased fatigue susceptibility.

Appendix: Crack velocity relations

We use a phenomenological velocity function $v\{G[K(c)], R\}$ to fit literature data for our glass systems, for incorporation into the differential equation for kinetic crack growth in the text.

The G range for our function is bounded by well defined values of the Dupré work of separation: W_0 in inert environment (as defined in Part I); and W_E in active environment, expressible as an isotherm equation [26]

$$W_E = W_{V(sat)} - A\ln(R) \quad \text{gas} \qquad \text{(A1a)}$$

$$W_E = W_L \quad \text{liquid} \qquad \text{(A1b)}$$

in the region $W_{V(sat)} \leqslant W_E < W_0$, where $W_{V(sat)}$ pertains to saturated vapour ($R = 1$) and W_L ($< W_{V(sat)}$) to liquid; $R(\leqslant 1)$ is the relative humidity and A a constant. The velocity function is a composite of relations in the following three regions of behaviour.

Region I. At low G the crack growth is governed by some interaction with environmental species and is accordingly sensitive to the concentration. It satisfies a relation of the kind

$$v_I = v_0 \sinh[B(G - W_E)] \quad G \geqslant W_E \qquad \text{(A2)}$$

where v_0 and B are constants for a given material–environment system. Note the provision for a threshold at $G = W_E$. (Strictly, at $G < W_E$, the possibility exists for $v_I < 0$ in reversible fracture, but we set $v_I = 0$ in this region on the grounds that reversible crack healing is unlikely to occur to any great extent in practical glass systems. [27])

Region II. At intermediate G the crack growth in gases is governed by diffusion of the environmental species along the interface. The relation is

$$v_{II} = DRG \qquad \text{(A3)}$$

with D a material constant [10, 26].

Region III. At high G the growth is independent of environment. It satisfies a relation of the same kind as Equation A2, but with very strong dependence on G. We simply approximate this function by a cut off velocity

$$v_{III} = v_T \qquad \text{(A4)}$$

at $G = W_0$, where $v_T \approx 1\ \text{km s}^{-1}$ is the speed of sonic waves.

The interaction and diffusion processes in regions I and II act in series, so the transition between these two regions takes the approximate composite form

$$1/v = 1/v_I + 1/v_{II} \qquad \text{(A5)}$$

Selected data for soda-lime glass [28] and fused silica [29] are plotted in Fig. A1. We mention that v–G

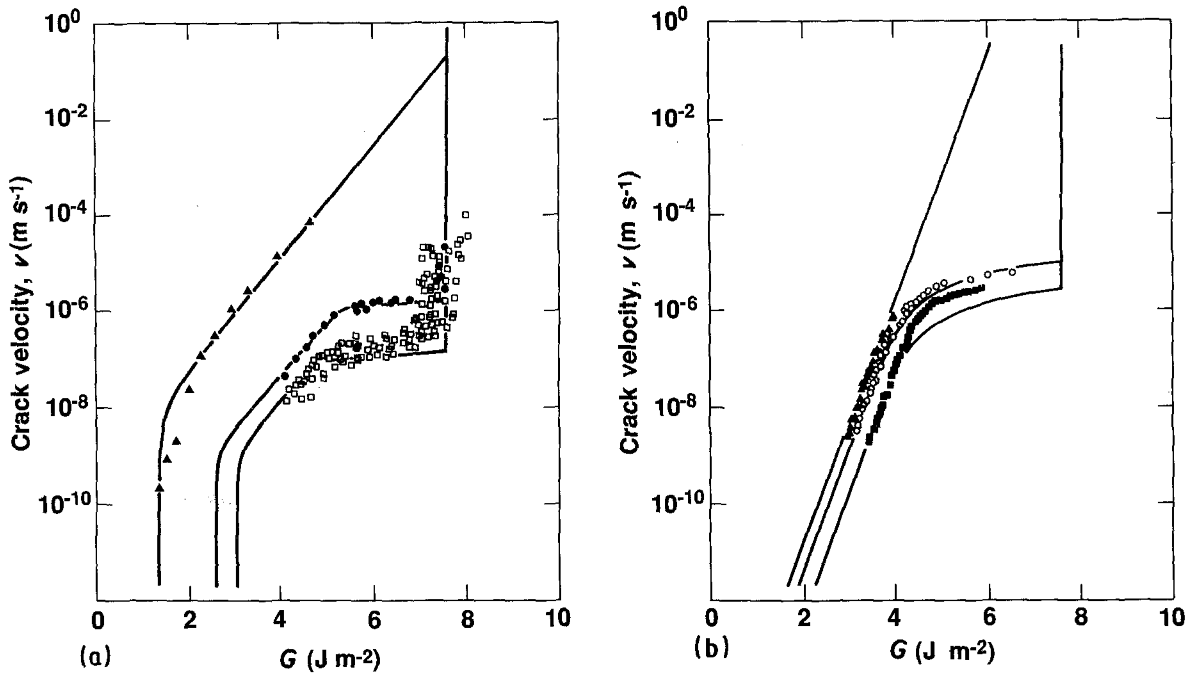

Figure A1 Crack velocity functions: (a) soda-lime glass, data from [27]; (▲ water, ● RH = 0.2%, □ RH = 0.017%) (b) fused silica glass, data from [28] (▲ water, ■ RH = 20%, ○ RH = 75%). Solid curves are fits to data using crack velocity functions in Appendix (see Table AI for fitted parameters).

TABLE AI Values of crack velocity parameters for glasses used in this study. From fits to data in Fig. A1

		Soda-lime	Fused silica
W_L	$(\mathrm{J\,m^{-2}})$	1.29	0.00
$W_{V(sat)}$	$(\mathrm{J\,m^{-2}})$	1.34	0.145
A	$(\mathrm{J\,m^{-2}})$	0.99	1.40
B	$(\mathrm{J\,m^{-2}})^{-1}$	2.60	5.83
D	$(\mathrm{m^3\,s^{-1}\,J^{-1}})$	1.07×10^{-4}	1.70×10^{-4}
v_0 (air)	$(\mathrm{m\,s^{-1}})$	2.56×10^{-9}	1.25×10^{-14}
v_0 (water)	$(\mathrm{m\,s^{-1}})$	2.02×10^{-8}	1.25×10^{-14}

data of this type are notoriously variable – reproducibility of an order of magnitude on any given material in any given environment, even in the same laboratory by the same worker using the same test geometry, is the exception rather than the norm. The full curves represent fits to these data, in accordance with Equations A1 to A5. Parameters resulting from these fits are listed in Table A1.

Acknowledgements

The authors are grateful to S. R. Choi, K. Jakus and J. E. Ritter for discussions and for permission to reproduce data from their laboratory, and to K.-T. Wan and S. Line for assistance with the computations. This work was supported by a grant from E. I. Du Pont de Nemours and Co.

References

1. S. LATHABAI, J. RöDEL, T. P. DABBS and B. R. LAWN, *J. Mater. Sci.*, **26** (1991) 2157.
2. B. R. LAWN, T. P. DABBS and C. J. FAIRBANKS, *ibid.* **18** (1983) 2785.
3. H. MULTHOPP, B. R. LAWN and T. P. DABBS, in "Deformation of Ceramic Materials II", edited by R. E. Tressler and R. C. Bradt (Plenum, New York, 1984) p. 681.
4. T. P. DABBS, B. R. LAWN and P. L. KELLY, *Phys. Chem. Glasses* **23** (1982) 58.
5. T. P. DABBS and B. R. LAWN, *ibid.* **23** (1982) 93.
6. T. P. DABBS, C. J. FAIRBANKS and B. R. LAWN, ASTM STP 844 (American Society for Testing and Materials, Philadelphia, 1984) p. 142.
7. B. R. LAWN, D. B. MARSHALL and T. P. DABBS, in "Strength of Glass", edited by C. R. Kurkjian (Plenum, New York, 1985) p. 249.
8. T. P. DABBS and B. R. LAWN, *J. Amer. Ceram. Soc.* **68** (1985) 563.
9. S. R. CHOI, J. E. RITTER and K. JAKUS, *ibid.*, **73** (1990) 268.
10. B. R. LAWN and T. R. WILSHAW, in "Fracture of Brittle Solids" (Cambridge University Press, London, 1975).
11. S. LATHABAI and B. R. LAWN, *J. Mater. Sci.* **24** (1989) 4298.
12. H. MULTHOPP and C. J. FAIRBANKS, Unpublished work.
13. T. P. DABBS and B. R. LAWN, *J. Amer. Ceram. Soc.* **65** (1982) C-37.
14. D. B. MARSHALL and B. R. LAWN, *ibid.* **63** (1980) 532.
15. T. P. DABBS, PhD Thesis, University of New South Wales, Australia (1984).
16. J. E. RITTER, J. M. SULLIVAN and K. JAKUS, *J. Appl. Phys.* **49** (1978) 4779.
17. H. C. CHANDAN and D. KALISH, *J. Amer. Ceram. Soc.* **65** (1982) 171.
18. S. P. CRAIG, W. J. DUNCAN, P. W. FRANCE and J. E. SNODGRAS, presentation at ECOC Conference, Cannes, France, 1982.
19. S. M. WIEDERHORN and J. E. RITTER, ASTM STP 678 (American Society for Testing and Materials, Philadelphia, 1979) p. 202.
20. S. P. GUNSASEKERA and D. G. HOLLOWAY, *Phys. Chem. Glasses* **14** (1973) 45.
21. J. F. KRANICH and H. SCHOLZE, *Glasstechn. Ber.* **49** (1976) 135.
22. C. J. FAIRBANKS, R. S. POLVANI, S. M. WIEDERHORN, B. J. HOCKEY and B. R. LAWN, *J. Mater. Sci. Lett.* **1** (1982) 391.

23. A. ARORA, D. B. MARSHALL, B. R. LAWN and M. V. SWAIN, *J. Non-Cryst. Solids* **31** (1979) 415.
24. B. R. LAWN, A. G. EVANS and D. B. MARSHALL, *J. Amer. Ceram. Soc.* **63** (1980) 574.
25. H. M. CHAN and B. R. LAWN, *ibid.* **71** (1988) 29.
26. K.-T. WAN, S. LATHABAI and B. R. LAWN, *J. Eur. Ceram. Soc.* **6** (1990) 259.
27. B. STAVRINIDIS and D. G. HOLLOWAY, *Phys. Chem. Glasses* **24** (1983) 19.
28. S. M. WIEDERHORN, *J. Amer. Ceram. Soc.* **50** (1967) 407.
29. S. SAKAGUCHI, Y. SAWAKI, Y. ABE and T. KAWASAKI, *J. Mater. Sci.* **17** (1982) 2878.

Received 17 October 1989
and accepted 20 March 1990